CHEMISTRY OF MATERIALS

pubs.acs.org/cm Article

Optimized Cation Exchange for Mercury Chalcogenide 2D Nanoplatelets and Its Application for Alloys

Corentin Dabard, Josep Planelles, Hong Po, Eva Izquierdo, Lina Makke, Charlie Gréboval, Nicolas Moghaddam, Adrien Khalili, Tung Huu Dang, Audrey Chu, Stefano Pierini, Claire Abadie, Mariarosa Cavallo, Erwan Bossavit, Xiang Zhen Xu, Philippe Hollander, Mathieu Silly, Emmanuel Lhuillier, Juan I. Climente, and Sandrine Ithurria*

Cite This: *Chem. Mater.* 2021, 33, 9252−9261 Read Online

ACCESS | Metrics & More | Article Recommendations | Supporting Information

ABSTRACT: II−VI two-dimensional (2D) nanoplatelets (NPLs) exhibit the narrowest optical features among nanocrystals (NCs). This property remains true for Hg-based NPLs, despite a cation exchange procedure to obtain them from Cd-based NPLs, which leads to structural defects (poorly defined edges and voids) inducing inhomogeneous broadening. Here, we propose an optimized procedure for which a solvent, surface chemistry, and reaction conditions are rationally considered. The procedure is applied to the growth of alloyed $HgSe_{1-x}Te_x$ NPLs with various compositions. We report a bright photoluminescence for all compositions. Structural properties being now well defined, it is possible to study the electronic properties of these objects. To do so, we combine k·p modeling of quantum-confined structures with X-ray photoemission. In particular, we clarify the origin of the similarity between CdTe and HgTe NPLs absorption spectra despite their vastly differing bulk band structures. Finally, static- and time-resolved photoemission unveil a crossover from n- to p-type behavior in $HgSe_{1-x}Te_x$ NPLs while increasing the Te content.

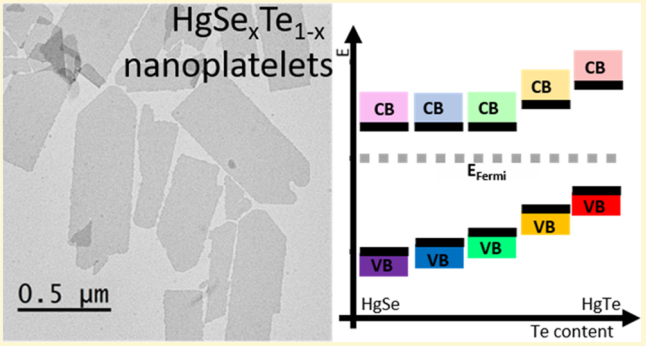

Downloaded via UNIV PARIS-SUD on February 18, 2022 at 14:31:03 (UTC).
See https://pubs.acs.org/sharingguidelines for options on how to legitimately share published articles.

INTRODUCTION

Among nanocrystals (NCs), two-dimensional (2D) nanoplatelets[1−3] (NPLs) offer a unique playground. Owing to well defined facets, the growth can be controlled up to the monolayer level.[4,5] Their photoluminescence (PL) spectrum is likewise one of the narrowest among NCs, and finally, the large particle volume reduces the Auger effect,[6,7] enabling high-performing light-emitting diodes[8−10] (LEDs) or low threshold lasers.[11−13]

Initially proposed for cadmium chalcogenides with a visible band gap, the concept of 2D NPLs has been extended to infrared materials such as lead[14−18] and mercury chalcogenides[19−24] (HgX). HgTe NPLs being obtained from Cd-based NPLs with an atomic layer control on the roughness, the associated PL signal is reported to be the narrowest among NC ones in the near IR. The synthesis of HgTe NPLs has already been established, however, it suffers from several issues. (i) First, the synthesis is not direct: HgTe NPLs are obtained from CdTe NPLs by cation exchange. As discussed later on, the current exchange conditions remain unoptimized, leading to poorly defined NPL edges and to the presence of holes; see the electron microscopy image in Figure 1c. (ii) Second, they lack from spectral tunability. Even though a red shift of the band edge can be obtained by modifying the surface chemistry,[20,24] only 3 monolayer NPLs have been reported so far (3 ML NPLs present 4 planes of cations alternated with 3 planes of chalcogens). Cation exchange appears to be self-limited to surface cadmium (likely due to the bulkiness of Hg cations and the topotaxial exchange), and attempts to perform cation exchange of thicker NPLs have led to core/shell structures, where the inner cadmium planes remain unaffected.[22] Moreover, while alloying,[25−27] doping[28−31] and electrical charging[32] appear as possible alternatives to quantum confinement to shift the spectral response for Cd-based NPLs; none of these strategies have been reported yet for Hg-based NPLs. (iii) Last, PL has only been reported for HgTe NPLs, while HgSe NPLs remained non emissive up to the recent demonstration of PL in core/shell structures.[33]

These restrictions call for an optimized procedure to obtain HgX NPLs. Here, we first highlight the limitations of the

Received: August 27, 2021
Revised: November 2, 2021
Published: November 29, 2021

© 2021 American Chemical Society

https://doi.org/10.1021/acs.chemmater.1c02951
Chem. Mater. 2021, 33, 9252−9261

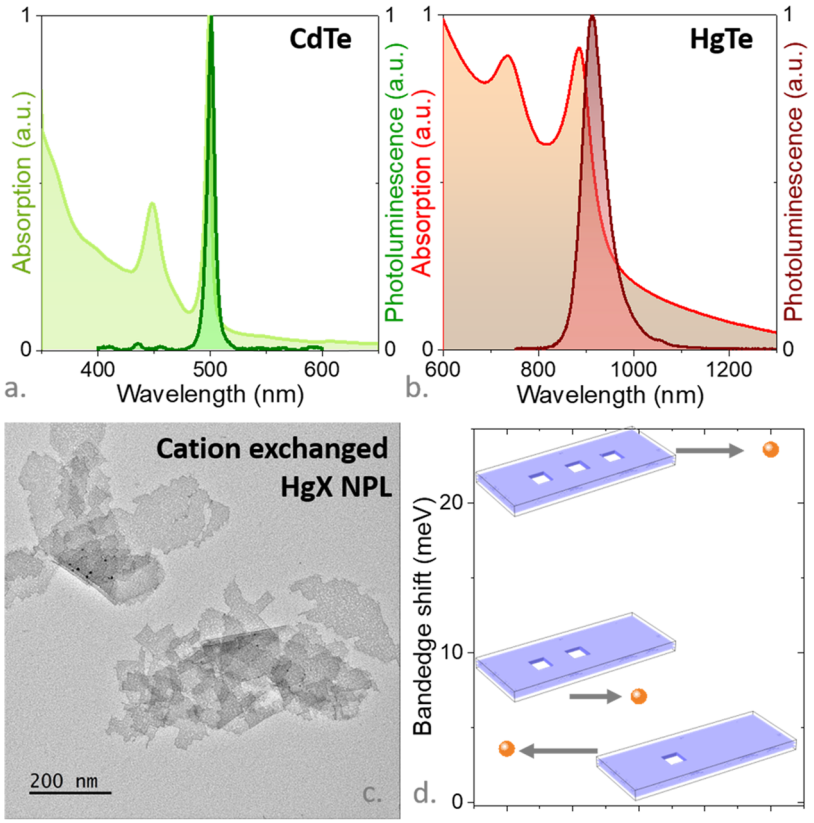

Figure 1. HgTe NPL growth using cation exchange. (a) Absorption and PL spectra of 3 ML CdTe NPLs. (b) Absorption and PL spectra of 3 ML HgTe NPLs. (c) Transmission electron microscopy (TEM) image of 3 ML HgX NPLs using the procedure from ref 18 (X: Se or Te or a mix). (d) Calculated shift of the band gap in the presence of geometric defects.

current procedure and show that cation exchange can affect the NPL morphology. Using k·p simulations, we unveil the influence of structural defects in the inhomogeneous broadening. We then propose an optimized procedure, where the solvent, the temperature, and the surface chemistry have been revisited. In a second step, we apply this procedure to the growth of alloyed $HgSe_{1-x}Te_x$ NPLs and show that all compositions can be obtained while preserving the NPLs morphology and their PL. Finally, we use k·p modeling, as well as, static- and time-resolved X-ray photoemission spectroscopy (TrXPS) to explore the electronic structure of $HgSe_{1-x}Te_x$ ML NPLs. We, in particular, reveal why the spectrum of HgTe(Se) NPLs looks similar—though shifted—to the one observed for CdTe(Se), while the bulk electronic structures are significantly different. Moreover, we bring evidence for a crossover from n-type to p-type as the composition of $HgSe_{1-x}Te_x$ NPL switches from Se rich to Te rich. Beyond the color change, this result is promising for the pn junction design that remains undemonstrated using NPLs.[34]

EXPERIMENTAL SECTION

Chemicals. Octadecene (ODE) (Sigma-Aldrich, 90%), dried cadmium acetate ($Cd(Ac)_2$) (Sigma-Aldrich, 99.995%), cadmium oxide (CdO) (Strem 99.99%), dodecanethiol (DDT, Sigma-Aldrich, 98%), 1,2-ethanedithiol (EDT, Fluka, 98%), mercury acetate ($Hg(Ac)_2$, Merck, 99%), myristic acid (Sigma-Aldrich 99%), propionic acid (Sigma-Aldrich 99%), sodium oleate (Sigma-Aldrich, >82%) selenium powder (Se) (Strem Chemicals 99.99%), tellurium powder (Te) (Sigma-Aldrich 99.99%), oleic acid (OA) (Sigma-Aldrich 90%), oleylamine (OLA, Acros, 80−90%), trioctylphosphine (TOP) (Alfa Aesar, 90%), chlorobenzene (CB, Alfa Aesar, 99%), chloroform (Carlo Erba), dichloromethane (DCM, Sigma-Aldrich, >99,8%), *n*-octane (SDS, 99%), tetrachloroethylene (TCE, VWR) toluene (VWR 99.5%), *n*-hexane (VWR 99%), and ethanol absolute (VWR) are used. All chemicals are used as received. As mercury compounds are highly toxic, they need to be handled with special care.

1M TOPTe. Te powder (2.54 g) is mixed with 20 mL of TOP in a three-neck flask. The flask is kept under vacuum at room temperature for 5 min before the temperature is increased to 100 °C. Degassing is conducted at this temperature for 20 min. Then, the atmosphere is switched to Ar and the temperature is increased to 275 °C. The solution is stirred until a clear orange coloration is obtained. The flask is afterward cooled to room temperature and the color turns yellow. Finally, this solution is transferred to a nitrogen-filled glovebox for storage.

1M TOPSe. Selenide powder (1.58 g) is mixed and stirred with 20 mL of TOP overnight until complete dissolution of selenium in the glovebox. This solution is stored inside the glovebox.

Cadmium Myristate. In a 50 mL three-neck flask, 2.56 g of CdO (20 mmol) and 11 g of myristic acid (50 mmol) are mixed and degassed for 30 min at 80 °C. Then, under an argon flow, the temperature is set to 200 °C until the solution becomes colorless. At 60 °C, 30 mL of methanol is added to solubilize the excess of myristic acid. Cadmium myristate is precipitated using a centrifuge tube with methanol. The washing process is repeated at least three times. The final powder is dried overnight under vacuum at 70 °C.

Cadmium Propionate. In a 100 mL three-neck flask, 5.18 g of CdO (40.3 mmol) and 50 mL of propionic acid are mixed and heated at 70 °C for 1 h under an argon atmosphere. When the entire solid is dissolved and a colorless solution is obtained, the heating is stopped and acetone is added to the precipitate cadmium propionate. The powder is centrifuged and washed at least three times with acetone and then set under vacuum overnight.

https://doi.org/10.1021/acs.chemmater.1c02951
Chem. Mater. 2021, 33, 9252−9261

$CdSe_{1-x}Te_x$ NPL Synthesis. In a 50 mL three-neck flask, 120 mg of $Cd(Myr)_2$ and 12 mL of ODE are mixed and degassed at room temperature for 30 min. The atmosphere is switched to argon and the temperature is increased to 230 °C. A mixture of 60 mg of $Cd(Ac)_2$ and 160 mg of $Cd(Prop)_2$ is added. After 1 min, a mixture of 150 μL of different ratios of TOPTe and TOPSe, 200 μL of OA, and 2 mL of ODE is added at a 8 mL·h^{-1} rate. After 30 min, the reaction is quenched by cooling and adding oleic acid. The NPLs are centrifuged twice with 15 mL of hexane and 15 mL of ethanol and then redispersed in 10 mL of hexane. Different ratios of Se/Te have been used to modify the composition of the NPLs and are in good agreement with the measure performed.

CdSe NPL Synthesis. In a 50 mL three-neck flask, 240 mg of $Cd(Ac)_2$ and 15 mL of ODE are mixed and degassed at 60 °C for 30 min. Under an argon flow, the temperature is set to 190 °C, and then, a mixture of 600 μL of TOPSe 1M, 200 μL of OA, and 5 mL of ODE is added dropwise at a 4 mL·h^{-1} rate. The mixture is then cooled to room temperature. The NPLs are centrifuged twice with 15 mL of hexane and 15 mL of ethanol and then redispersed in 10 mL of hexane.

CdTe NPL Synthesis. In a 100 mL three-neck flask, 390 mg of $Cd(Prop)_2$, 240 μL of OA, and 30 mL of ODE are mixed and degassed at 90 °C for 1 h. Under an argon flow, the temperature is set to 210 °C. Then, a mixture of 300 μL of TOPTe 1M and 1.5 mL of ODE is added to the mixture. After 30 min at 210 °C, the mixture is cooled and 1.7 mL of oleic acid is added. The NPLs are centrifuged twice with 15 mL of hexane and 20 mL of ethanol and then redispersed in 30 mL of hexane.

Optimized Cation Exchange Procedure. In a glass tube, 200 μL of $CdSe_{1-x}Te_x$ (4 μmol of Cd) redispersed in 3 mL of TCE is added. The tubes are stored in a fridge until the temperature reaches 5 °C. Then, 50 μL of $Hg(OA)_2$ (0.08 M in OA) and 2 equiv (for CdTe), 4 equiv (for $CdSe_{0.25}Te_{0.75}$), 6 equiv (for $CdSe_{0.5}Te_{0.5}$), 8 equiv (for $CdSe_{0.75}Te_{0.25}$), 10 equiv (for CdSe) of $Hg(Ac)_2$ (0.1M in OLAm; 1 equiv = 40 μL) are added. The reaction is complete when the absorption features stabilize. The NPLs are then precipitated by adding a few drops of ethanol and centrifuged at 12 000 rpm for 1 min. The NPLs are finally suspended in 1 mL of TCE.

Absorption Spectroscopy. UV−visible spectra were obtained using a Cary5000 spectrometer.

Photoluminescence Spectroscopy. Photoluminescence and excitation spectra were obtained with an Edinburgh Instrument spectrometer. During the measurements, the NPLs were dispersed in TCE.

Photoluminescence Quantum Yield (PLQY). The PLQY of HgTe NCs in solution was obtained using an Edinburgh Instrument spectrometer equipped with an integrating sphere. The samples were excited at 700 nm with a Xe lamp, and the photons were collected with an InGaAs detector cooled with liquid N_2.

Diffraction. X-ray diffraction (XRD) pattern is obtained by drop-casting the solution of nanocrystals on a Si wafer. The diffractometer is a Philips X'Pert, based on the emission of the Cu Kα (λ = 0.154 nm) line, operated at 40 kV and 40 mA current.

Elemental Analysis Using X-ray Dispersive Spectroscopy (EDX). For EDX analysis, the particles are spread on a conductive carbon tape. The EDX analysis is performed using an FEI Magellan scanning electron microscope, operated at 15 kV and 1.6 nA. The X-ray analysis is made with an Oxford probe.

TEM. A drop of diluted NC solution was drop-casted onto a copper grid covered with an amorphous carbon film. The grid was degassed overnight under secondary vacuum. Imaging was conducted using a JEOL 2010 transmission electron microscope, operated at 200 kV.

X-ray Photoemission Measurements. For photoemission spectroscopy, we use the Tempo beamline of synchrotron SOLEIL. Films of nanocrystals are spin-casted onto a gold-coated Si substrate (the gold layer was 80 nm thick). The ligands of the NPLs are exchanged with ethandithiol using the same procedure for device fabrication to avoid any charging effects during measurements. Samples are introduced in the preparation chamber and degassed until a vacuum below 10^{-9} mbar is reached. Then, samples are introduced in the analysis chamber. The signal is acquired using an MBS A-1 photoelectron analyzer equipped with a delay line detector developed by Elettra.[35] Acquisition is done at a constant pass energy (50 eV) within the detector. A photon energy of 150 eV is used for the acquisition of valence bands and work functions, while a 600 eV photon energy is used for the analysis of the core levels. A gold substrate is used to calibrate the Fermi energy. The absolute value of the incoming photon energy is determined by measuring the first and second orders of Au4f core level peaks. Then, for a given analyzer pass energy, we measure the Fermi edge and set its binding energy as zero. The same shift is applied to all spectra acquired with the same pass energy. To determine the work function, we apply an 18 V bias, whose exact value has been determined by looking at the shift of the Fermi edge.

Time-Resolved X-ray Photoemission Spectroscopy Measurements (TrXPS). The sample is excited by a 405 nm pulsed laser diode. The pulse duration is around 40 μs. The output equivalent CW power used for the experiment is 100 mW and the beam spot is typically 300 × 300 μm^2 (synchrotron beam) and 400 μm × 2 mm (laser beam). The laser beam is spatially aligned to overlap with the synchrotron beam on the sample holder. The pump−probe TrXPS is conducted in a stroboscopic configuration, where the temporal resolution is given by the time response of the photoemission analyzer. The latter is estimated to be 30 ns, limited by the spread of the electrons between the hemispheres. Then, the photoemission spectrum of a given core level is acquired every 10 ns. Each spectrum of the series is fitted by two Gaussians to extract the kinetic energy of each peak. This procedure enables to follow energy shifts as small as 5 meV.

k·p Modeling. The electronic structure is calculated using the three-dimensional (3D), 8-band k·p model for zinc-blende semiconductors grown along [001], as proposed by Novik and co-workers.[36] HgTe parameters are taken from the same source,[36] and HgSe parameters are taken from ref 37. The NPL is modeled as a cuboidal box with a finite confinement potential of 4 eV outside the inorganic region. Excitonic effects are disregarded on account of the large effective Bohr radius (tens of nanometers). The resulting states are then multicomponent spinors of the form $\Psi(r) = \sum_{n=1}^{8} f_n(r)u_n(r)$, where $f_n(r)$ is the envelope function associated with the periodic Bloch function $u_n(r)$. The latter corresponds to states at the Γ point, $u_n(r) = |\Gamma, j_z\rangle$, with Γ indicating the band symmetry and j_z indicating the Bloch angular momentum projection. Specifically, we considered $u_1(r) = |\Gamma_6, +1/2\rangle$ and $u_2(r) = |\Gamma_6, -1/2\rangle$—which we refer to as "electron" bands by analogy with the conduction band of most II−VI zinc-blende semiconductors—$u_3(r) = |\Gamma_8, +3/2\rangle$ and $u_4(r) = |\Gamma_8, -3/2\rangle$—heavy hole (HH) bands—$u_5(r) = |\Gamma_8, +1/2\rangle$ and $u_6(r) = |\Gamma_8, -1/2\rangle$—light hole (LH) bands, and $u_7(r) = |\Gamma_7, +1/2\rangle$ and $u_8(r) = |\Gamma_7, -1/2\rangle$—split-off (SO) bands. The weight of a given band within $\Psi(r)$ is estimated from $\langle f_n|f_n\rangle$. For quantum well simulations, in-plane wave vectors are set to $k_x = k_y = 0$ (sub-band edge), which makes the Hamiltonian one-dimensional. In this case, the 8-band Hamiltonian decouples into two 1-band Hamiltonians (for heavy holes with either spin) plus two 3-band Hamiltonians (coupling electron, light hole, and split-off sub-bands with the same spin). Absorption spectra are calculated using the Fermi golden rule within the dipole approximation, considering intra- and interband terms. This provides the δ-like peaks in Figure 4d, which correspond to the onset of a quantum well sub-band. To simulate the complete quantum well absorption, the peaks are broadened using Lorentzian functions with a phenomenological width of 50 meV, which accounts for the coupling to phonons, size dispersion, etc. Also, the absorption beyond the band edge (i.e., finite in-plane wave vectors) is accounted for by adding a Fermi function at 300 K. The height of this function is taken to be half that of the sub-band edge peak, which is a phenomenological representation of the lack of excitonic interactions in the continuum. In 3D simulations (Figure 1), the γ parameter γ_3 is set to 0.9 (instead of 1.3) to grant ellipticity of the differential equation system, hence avoiding spurious states. We have tested that this has a minor influence on the energies.

https://doi.org/10.1021/acs.chemmater.1c02951
Chem. Mater. 2021, 33, 9252−9261

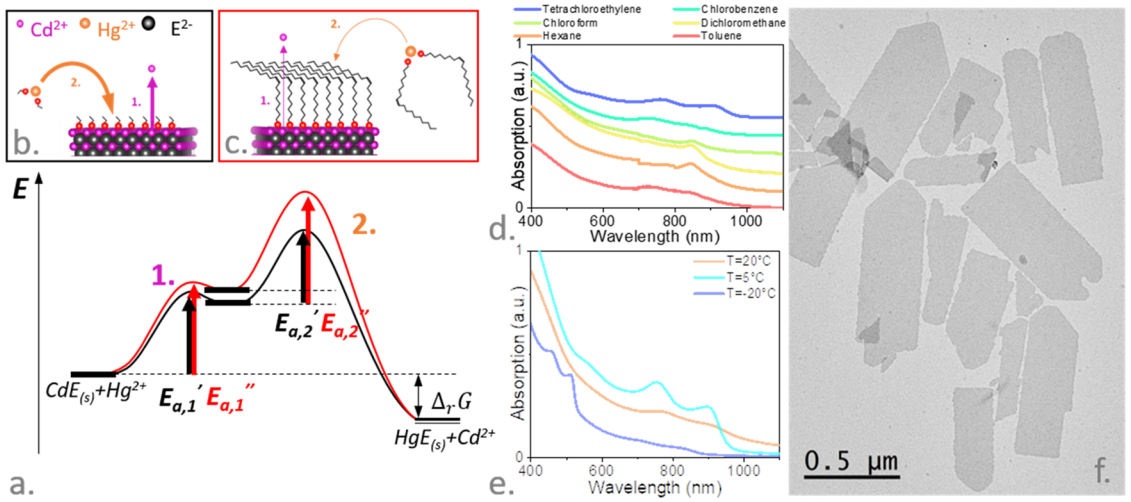

Figure 2. Optimized cation exchange procedure. (a) Energetic profile of the cation exchange procedure from CdTe to HgTe NPL with two potential barriers. The first barrier relates to the diffusion of Cd ions toward the surface and through the ligand shell while the second results from the Hg ion migration up to and within the NPL. (b) Scheme of the cation exchange procedure conducted with nonbulky precursors; Cd^{2+} ions easily come out, and Hg^{2+} ions have fast access to the surface of the NPL. (c) Scheme of the cation exchange procedure conducted with bulky precursors; Cd^{2+} extraction is slowed down by capping ligands, and Hg^{2+} ion approach is also slowed down due to lower diffusivity of the bulky ions. (d) Absorption spectra of $HgSe_{0.5}Te_{0.5}$ NPLs while cation exchange is conducted, at room temperature, in various solvents; see associated TEM pictures in Figure S2. (e) Absorption spectra of the $HgSe_{0.5}Te_{0.5}$ NPLs while cation exchange is conducted at various temperatures in TCE. (f) TEM image of $HgSe_{0.5}Te_{0.5}$ NPLs obtained with an optimized cation exchange procedure.

RESULTS AND DISCUSSION

To understand the need for an optimized growth of HgX NPLs, we start by discussing the limitations of the current method.[19] HgTe NPLs are obtained using a two-step procedure. First, CdTe NPLs of 3 MLs are synthesized using the procedure by Pedetti et al.[38] They display an energy band edge at 500 nm (2.47 eV), associated with an extremely narrow PL signal (30 meV for full width at half-maximum), with a weak Stokes shift compared to the absorption edge; see Figure 1a. These NPLs, suspended in toluene, are then exposed to Hg^{2+} cations, through mercury salt ($Hg(Ac_2)$) dissolved in oleylamine. The presence of amines is essential to preserve the 2D aspect of the NPLs. With their bulky lateral chains, long aliphatic chain amines are used to slow down the reaction and avoid the shape reconstruction.[19] During the cation exchange procedure, the absorption band edge first disappears before being recovered with a strong red shift (PL at 912 nm or 1.35 eV with a 50 meV Stokes shift); see Figure 1b. Transmission electron microscopy (TEM) reveals that, indeed, the 2D shape is preserved, but the morphology is partly damaged. The edges of NPLs have a fractal structure and voids are present in the inner part of NPLs; see Figure 1c.

This change of morphology also impacts the spectroscopic properties of NPLs. The ratio of full width at half-maximum over the PL peak energy increases from 1.2% for CdTe NPLs to 6% for HgTe NPLs. Moreover, although the Stokes shift is very weak in the case of 3 ML CdTe NPLs, it is clearly observed for 3 ML HgTe NPLs. To better relate this change of band morphology to the spectroscopic changes, we then model the electronic structure of HgTe NPLs using k·p modeling. A cuboidal NPL with dimensions $50 \times 20 \times 1$ nm^3 is considered. It corresponds to the smallest NPLs observed in our samples. We then compare the band gap in absence and presence of surface defects, which are modeled as small hole(s) in the NPL, whose surface is 5×5 nm^2; see Figure 1d. If the number of defects is small and off-centered, the impact on the band gap energy is minor (few meV shift $\ll k_bT$ or NPL PL line width; see the leftmost result in Figure 1d). However, an increasing number of defects, and/or their presence near the NPL center, efficiently reduces the area available for the exciton, introducing lateral confinement and hence a blue shift of the band gap energy (mid- and rightmost results in Figure 1d).

To rationalize the cation exchange procedure, we can decompose this process in two steps. First, the Cd^{2+} ions have to diffuse out of the NPL, and then Hg^{2+} ions diffuse to the surface and finally within the NPL; see Figure 2b. Thus, the energetic path corresponding to the reaction can be associated with two energetic barriers;[39] see Figure 2a. To preserve quasi-equilibrium conditions that will prevent a surface reorganization during the reaction, our strategy consists in slowing down the reaction. It has been previously demonstrated by Izquierdo et al.[19] that long aliphatic chain amines (oleylamine) slow down the cation exchange procedure compared to moderate length amines ((tri)octylamine). This strategy allows to minimize the disturbance of the anion lattice during the exchange procedure. To do so, we tune three experimental conditions: (i) temperature, (ii) solvent, and (iii) ligands.

First, one can play on the global system energy through the temperature. The usual procedure is conducted at room temperature. We thus performed the reaction at 5 and −20 °C; see Figure 2e. When the temperature is too low (i.e., −20 °C), the reaction is quenched and the 3 ML CdTe NPLs excitonic features are not fully transformed into 3 ML HgTe NPLs features: there is a kinetic freeze; see Figure S4. However, an intermediate temperature (+5 °C) enables a full cation exchange and the formation of HgTe NPLs with well-defined optical features and low diffusion at long wavelengths.

A second strategy to slow down the reaction is to change the solvent. The latter is involved during the cation exchange[40,41] by solubilizing or not the exchanged cations. We thus screen a series of solvents to observe their influence on the final materials; see Figures 2d, S2, and S3. For most of them, we observe a clear tail of absorption at wavelengths beyond the

https://doi.org/10.1021/acs.chemmater.1c02951
Chem. Mater. 2021, 33, 9252−9261

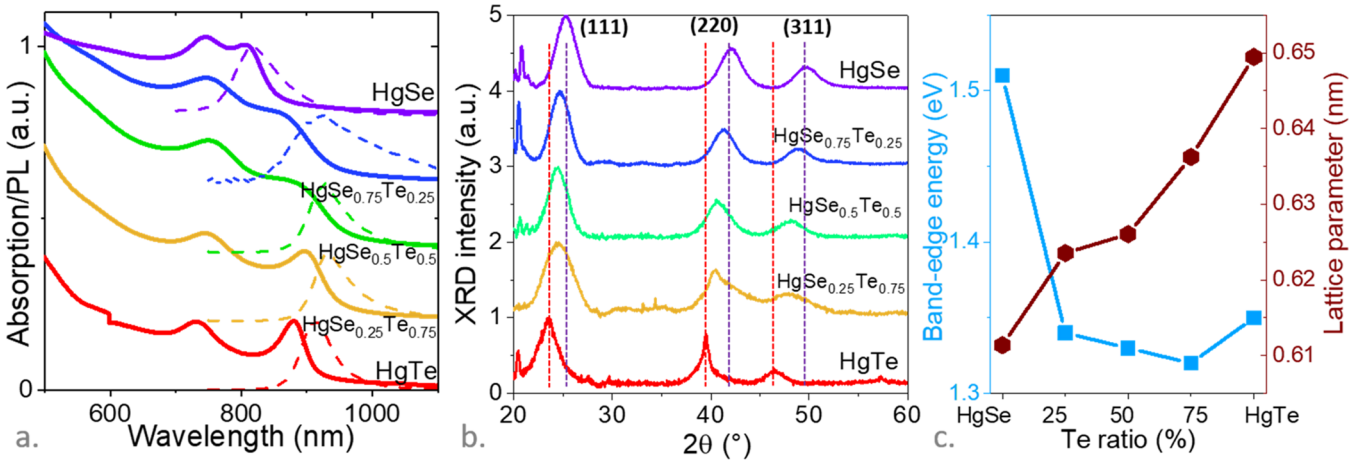

Figure 3. Spectroscopic and structural properties of alloyed $HgSe_{1-x}Te_x$ NPLs. (a) Absorption (solid lines) and PL (dashed lines) spectra of $HgSe_{1-x}Te_x$ NPLs with various compositions. For the sake of clarity, the spectra of various compositions have been vertically shifted. (b) X-ray diffraction pattern for a film made of $HgSe_{1-x}Te_x$ NPLs with various compositions. For the sake of clarity, the diffractograms of various compositions have been vertically shifted. Vertical dashed lines are here as guide lines of the peak positions for zinc-blende HgTe (red lines) and HgSe (blue lines) of lattice parameters a_{HgTe} = 0.65 nm and a_{HgSe} = 0.61 nm. (c) Band edge energy and lattice parameter of HgSeTe NPLs as a function of the Te content.

excitonic peak. Consistently with previous works, solvents such as chloroform completely etch the NPLs;[42] see Figure S2. Tetrachloroethylene (TCE) leads to the best performance while preserving the shape of the NPLs (Figure 2f) and with better-defined excitonic features, especially in the case of CdSe NPLs; see Figure 2d. We correlate this to the slower reaction kinetics observed in this solvent; see Figure S3. Through its chloride atoms, the TCE brings the presence of a soft base inside the system leading to a better solvation of the Hg^{2+} cation, making cation exchange less thermodynamically favorable.

Keeping this idea of cation solvation, we also change the ligands introduced during the exchange to affect the reaction kinetics. To begin with, the ligands located in the coordinating sphere of the incoming cations make it more bulky (similar to what was previously observed in the case of oleylamine). These ligands also lead to a modification of the surface chemistry and eventually an increase in steric hindrance on the NPLs surface. Both phenomena induce an increase in the energetic barrier to overcome and hence a slowdown in the cation diffusion toward the NPL surface; see Figure 2a−c. We demonstrate this trend using oleate as a bulky ligand; see Figure S6. Similar to the effect of temperature, there is a trade-off in the introduction of oleate. While no oleate leads to poorly defined NPLs, an excess of it quenches the reaction and prevents the transformation of CdTe NPLs into HgTe NPLs; see Figure S6. We also notice that the introduction of oleates has a beneficial role to stabilize the NPL surface; see Figure S5. In particular, oleate helps to better preserve the excitonic features after the NPL washing steps (Figure S5a), while TEM pictures show that in the presence of oleate, the edges of the NPL are preserved.

To summarize, we now update the cation exchange procedure while conducting it into tetrachloroethylene at a reduced temperature (+5 °C), in the presence of oleate. In the following, we apply this procedure to a series of 3 ML $CdSe_{1-x}Te_x$ NPLs, whose ratio x in Te is tuned from 0 to 1 by steps of 25%; see Figure S1 and Table S1 for the properties of $CdSe_{1-x}Te_x$ NPLs. TEM reveals that $HgSe_{1-x}Te_x$ NPLs mostly lie flat on the substrate the substrate, in comparison with $CdSe_{1-x}Te_x$ NPLs that can easily roll on themselves; see Figure S7. The absorption and PL spectra of $HgSe_{1-x}Te_x$ NPLs are given in Figure 3a and Table S2. All of them present well-defined absorption edges and luminescence properties. It is worth pointing that PL efficiency was too weak to be measured with the early cation exchange procedure[19] in the case of HgSe, while with the optimized procedure, the PL quantum yield span from 5 to 15% depending on the Se content. It is also worth mentioning that, contrary to our expectations, the line width of the final NPLs is not narrower with this optimized procedure, and we even notice a small increase from 60 to 80 meV of the full width at half-maximum. This increase actually reflects that, using the optimized procedure, NPLs are finally capped by a mixture of amines and oleates, while surface chemistry can strongly affect the final exciton energy by finely tuning the actual wave function delocalization.

To confirm the alloy character of the NPLs, we use X-ray diffraction (XRD) and photoemission spectroscopy (XPS). XPS (Figures 5a and S10) confirms the presence of Se and Te atoms in alloyed NPLs. On XRD patterns, the diffraction peaks of the zinc blende structure shift to smaller angles as the Te content increases in NPLs (Figure 3b). It is associated with a continuous increase of the lattice parameter while changing the composition of $HgSe_{1-x}Te_x$ NPLs from HgSe to HgTe (Figure 3c). This shift explains the rate increase observed during cation exchange as the Te content increases. Indeed, this process is sensitive to the diffusion of the cation inside the NPL, and thus, a larger lattice parameter should induce a faster diffusion; see Figure S8. In addition, the fact that we observe a shift of the peak rather than a doublet of peaks confirms the homogeneous composition of the alloy in NPLs. Interestingly, the band gap shift, contrary to the lattice parameter shift, is nonlinear with the NPL composition. The latter effect, called the bowing effect, has been previously observed on $CdSe_{1-x}Te_x$ NPLs.[26] The bowing factor is estimated to be b = 0.36 eV for $HgSe_{1-x}Te_x$ alloyed NPLs; see Figure S9. The band gap of $HgSe_{1-x}Te_x$-alloyed NPLs is very close to the one observed for the HgTe NPLs, even for high Se contents. On the other hand, the line width is affected by the Te content, and alloyed NPLs tend to present broader PL.

https://doi.org/10.1021/acs.chemmater.1c02951
Chem. Mater. 2021, 33, 9252−9261

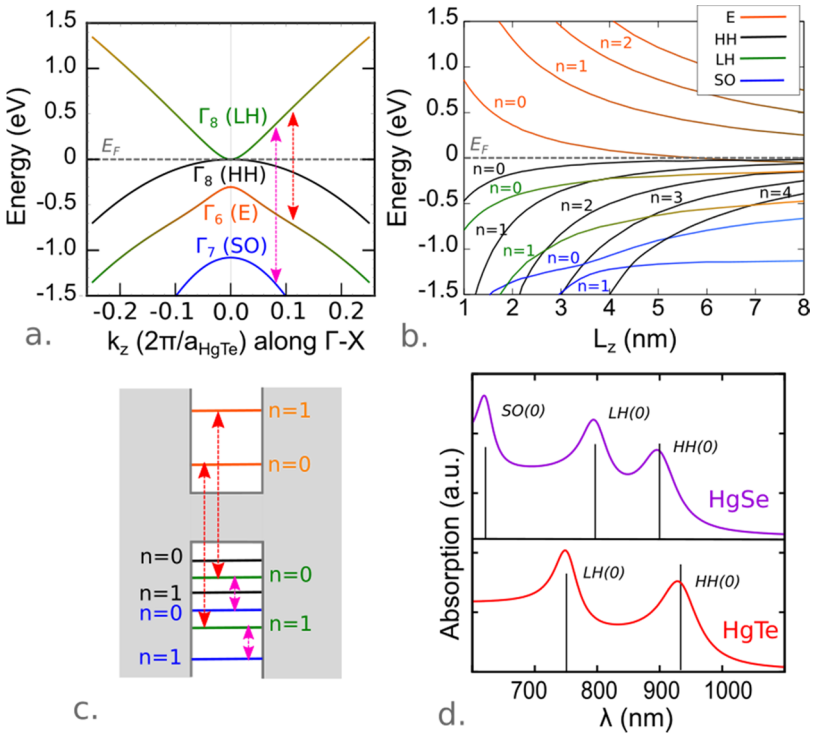

Figure 4. Band structure of HgTe and HgSe NPLs. (a) Dispersion diagram of bulk HgTe around the center of the Brillouin zone (Γ point). The labels give the symmetry in the double group of T_d at Γ ($k = 0$). Vertical arrows indicate interacting bands away from $k = 0$. (b) Energy of HgTe quantum well sub-bands as a function of the well thickness, with n the number of nodes along the confined dimension. In panels (a) and (b), E_F is the bulk Fermi level and the line colors denote the band composition. (c) Schematic of the band mixing taking place in quantum-confined systems. Vertical arrows indicate interacting sub-bands. (d) Calculated absorption spectrum of HgSe (top) and HgTe (bottom) for 1 nm thick wells. Vertical lines show the onset of sub-band absorption and its oscillator strength.

To better understand the photophysics of HgTe and HgSe NPLs, their band structure is analyzed using k·p Hamiltonians. Studies on the band structure of epitaxially grown HgTe quantum wells are available in the literature,[43−45] but these are few nanometer thick objects with moderate band offsets. By contrast, the NPLs we synthesize are in a much stronger quantum confinement regime, which calls for a specific assessment. For the present discussion, we focus on HgTe NPLs but the same observations hold for HgSe NPLs; see Figure S11.

Figure 4a shows the band dispersion of bulk HgTe near the center of the Brillouin zone, calculated with an 8-band k·p Hamiltonian. At the Γ point, the semimetal nature is clearly observed, with degenerate p-like Γ_8 (heavy hole, HH and light hole, LH) bands leaving a zero band gap. The s-like Γ_6 band, which forms the electron (E) conduction band in most zinc-blende semiconductors is, here, below the Fermi level, thus providing the characteristic band inversion of mercury chalcogenides. Away from the Γ point (i.e., when $k \neq 0$), the LH band starts coupling with E and split-off (SO) bands through the Kane parameter, as indicated by the vertical arrows. A first approximation of the band structure of HgTe NPLs was given within this bulk model,[23] assuming that the measured optical gap of 1.35 eV could be associated with a wave vector of $k \approx 0.2 \times (2\pi/a_{HgTe})$, where a_{HgTe} is the lattice constant. This resulted in severe band coupling, with the conduction band having comparable LH and E characters (notice the blended green and orange colors in Figure 4a). Here, we revise this conclusion using a truly quantum-confined model. The lack of translational symmetry along the direction of strong confinement of the NPL implies that the wave vector k_z is no longer a good quantum number, and it must be replaced by a momentum operator. A one-dimensional quantum well Hamiltonian is then obtained, which has been proved successful in describing the photophysics of CdSe NPLs.[46] Figure 4b shows that the HgTe sub-bands calculated with such a Hamiltonian are strongly influenced by the NPL thickness, L_z. A transition from semimetal to semiconductor takes place at $L_z \approx 6$ nm, with a band gap opening around the Fermi level. For $L_z = 1$ nm, the gap reaches 1.3 eV, in close agreement with our experiments.

Even though the eigenstates of the quantum well Hamiltonian are formed by a mixture of bands, we find that states above the Fermi level (E_F) have mainly E-band character, with an increasing number of nodes in the confined direction (n = 0,1,2,...). Likewise, states below E_F show a dominant HH, LH, or SO character. The mixing is weak compared to the bulk approach,[23] and the thinner the NPL, the weaker the mixing. For HgTe NPLs with $L_z = 1$ nm, which is the experimental regime, the conduction band ground state is 85% E-band. More details on the wave functions and band weights as a function of the NPL thickness are given in Figures S11 and S12.

The relative purity of the sub-bands near the Fermi level (E_F) for thin NPLs can be understood from simple selection rules. In the one-dimensional (1D) 8-band k·p Hamiltonian, E and LH bands are coupled by the linear momentum operator p_z.[36] This operator is antisymmetric with respect to the inversion along [001]. On the other hand, envelope functions with even (resp. odd) number of nodes are symmetric (resp. antisymmetric). Therefore, the matrix elements $\langle f_E^{n'}|p_z|f_{LH}^{n}\rangle$ are only finite if n and n' have opposite parity (e.g., $n = n' + 1$).

https://doi.org/10.1021/acs.chemmater.1c02951
Chem. Mater. 2021, 33, 9252−9261

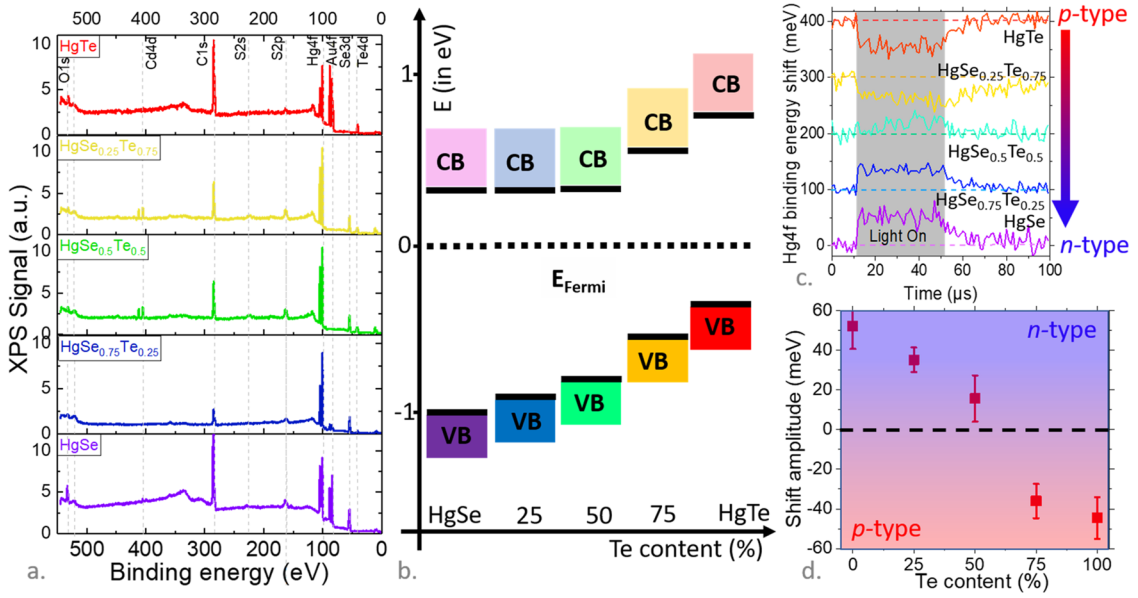

Figure 5. Electronic properties of $HgSe_{1-x}Te_x$ NPLs with various compositions. (a) X-ray photoemission overview spectra for $HgSe_{1-x}Te_x$ NPLs with various compositions. Analysis of the core levels are given in Figure S8. (b) Band alignment of $HgSe_{1-x}Te_x$ NPLs with various compositions. Analysis of the valance bands are given in Figure S12. (c) Temporal shift of the binding energy of the Hg 4f states from $HgSe_{1-x}Te_x$ NPLs with various compositions, followed by XPS while sample is illuminated by a pulse of light at 405 nm. The dashed lines are base lines. (d) Shift of the Hg 4f binding energy measured by TrXPS as a function of the Te content for $HgSe_{1-x}Te_x$ NPLs.

Similar reasoning for the coupling between LH and SO bands, which is mediated by p_z^2, shows that in such a case, n and n' must have the same parity (e.g., $n = n'$). These symmetry considerations lead to the scheme of sub-band coupling depicted in Figure 4c. One can notice that the lowest E state ($n = 0$) couples to the first LH state with one node ($n = 1$). Because quantum confinement is very strong in the NPL, the $n = 1$ LH state is far in energy, which makes the coupling weak.

The electronic structure described above gives rise to the absorption spectra plotted in Figure 4d, which we calculated for HgTe and HgSe NPLs with $L_z = 1$ nm. All transitions involve E ($n = 0$) as the final state, and they arise—from the longest to the shortest wavelength—from the HH ($n = 0$), LH ($n = 0$), and SO ($n = 0$) sub-bands. This spectral assignment is very similar to that of usual metal chalcogenide NPLs, such as CdTe and CdSe,[46−48] in spite of HgTe and HgSe having qualitatively singular band structures in bulk.

Now that the optical spectrum of NPLs is unveiled, we still have to address its absolute energy (i.e., vs vacuum level), which appears as a critical parameter for later integration of NPLs into devices. As already stated, the presence of both Se and Te is confirmed by XPS (Figure 5a). We also notice the presence of S atoms coming from the thiol ligands used to make the film of NPLs conductive and to avoid charging effects. Note that the oxygen contribution is very weak despite the air preparation of the samples, we can confidently exclude any oxidation of NPLs. On the other hand, C 1s contribution is clearly visible and results from the capping ligands. Hg 4f states display a strong contribution around 99 eV in binding energy with low effects from the Se content; see Figure S10. A small Cd contribution (Cd 4d state at around 405 eV) is also visible but its presence is not systematical, confirming that most Cd has been suppressed during the cation exchange procedure.

We then have a deeper look at the material band alignment; the photoemission signal from the cutoff of secondary electrons and valence band are given in Figure S14. In this case, the samples are capped with shorter thiol ligands not only to avoid charging effects during the XPS measurement but also to be more representative of conductive films used in devices. The band gap of the material capped with thiols is red-shifted with respect to the NPL capped with oleate/amine ligands; see Figure S13 and Table S3. For example, HgTe band edge is shifted from 1.35 to 1.17 eV. Considering this new band gap for each material and the relative energy of their valance band with respect to the Fermi level, we establish the band diagram of $HgSe_{1-x}Te_x$ NPLs as a function of the Te content; see Figure 5b. The Fermi level shifts from the upper part to the bottom part of the band gap as the Te content increases while remaining in the band gap. Thus, we can anticipate a change from n-type to p-type as the Te content increases, as further discussed later. Another striking feature that we can observe is a larger shift of the valence band than the conduction band. This behavior contrasts with the one observed for size dependence of HgTe.[49] Indeed, in HgTe, because of the large asymmetry between the hole and the electron[23] ($m_h^*/m_e^* \approx 25$ with m_h^* and m_e^* the hole and electron effective mass), the quantum confinement mostly affects the conduction band. In mercury chalcogenides, the valence band (Γ_8-HH) is mostly made of p-type chalcogenide orbitals, and the large change of valence band energy upon alloying thus reflects the difference of work function between Se and Te.[50] In this sense, alloying offers a complementary way to tune the band alignment while keeping the band gap slightly unaffected.

To confirm the crossover from n- to p-type, we used time-resolved X-ray photoemission spectroscopy (TrXPS). It is a pump−probe approach, where a laser pulse at 405 nm (3 eV to 40 μs pulse duration) excites the NPLs and the synchrotron beam probes the core level. As light is absorbed, the band bending of the surface of the sample is partly reduced, which results in a shift of the core level binding energy. In particular, this method is a convenient strategy to determine the nature of

https://doi.org/10.1021/acs.chemmater.1c02951
Chem. Mater. 2021, 33, 9252−9261

the majority carrier in a semiconductor sample.[20,21,35,51−53] A negative (i.e., reduction of the binding energy) shift under illumination is the signature of a downward band bending and is consistent with a p-type interface, while an increase of the binding energy is assigned to a n-type interface. Here, we follow the Hg 4f states while the $HgSe_{1-x}Te_x$ NPLs are illuminated; see Figure 5c. We notice a change from a positive to a negative shift as the Te content increases; see Figure 5c,d. This is consistent with static photoemission measurements, even if they do not probe the same effect: p-type nature is observed for the Te content >50% while samples with a high Se content are n-type. Given the weak change of band gap with alloying this approach is of utmost interest to build a pn junction.

CONCLUSIONS

We have shown that the previous procedure to grow HgTe and HgSe NPLs was suffering from key limitations and, in particular, a lack of PL in the case of HgSe NPLs. Moreover, the cation exchange leads to a shape reconstruction of NPLs and tends to broaden the optical features as revealed by the k·p model. We then propose an optimized procedure, where cation exchange is slowed down. To reach this goal, the reaction has to be conducted at low temperatures (5 °C), using TCE as a solvent and oleates as ligands. This leads to void-free NPLs with well-defined edges with reduced postexciton absorption. The procedure is then applied to alloys of $HgSe_{1-x}Te_x$. Thanks to this optimized procedure, all compositions now present PL, while the alloyed nature is confirmed by XRD. Since NPLs are obtained with a better-defined structure, it is now possible to discuss more clearly their electronic structure. In this regard, we show that the strong quantum confinement and inversion symmetry of NPLs induce the same transitions in Hg- and Cd-based NPLs. It explains a similar spectral shape for the two NPLs despite different bulk band structures. Finally, XPS unveils a crossover from n- to p-type in $HgSe_{1-x}Te_x$ NPLs, while the Te content is increased.

ASSOCIATED CONTENT

Supporting Information

The Supporting Information is available free of charge at https://pubs.acs.org/doi/10.1021/acs.chemmater.1c02951.

Extra material discussing: (i) CdSeTe NPL growth, (ii) optimized cation exchange procedure, (iii) alloyed HgSeTe NPL, (iv) k·p modeling of HgTe and HgSe NPLs, and (v) band alignment of HgSeTe NPLs (PDF)

AUTHOR INFORMATION

Corresponding Author

Sandrine Ithurria − *Laboratoire de Physique et d'Etude des Matériaux, ESPCI-Paris, PSL Research University, Sorbonne Université Univ Paris 06, CNRS UMR 8213, 75005 Paris, France;* orcid.org/0000-0002-4733-9883; Email: sandrine.ithurria@espci.fr

Authors

Corentin Dabard − *Laboratoire de Physique et d'Etude des Matériaux, ESPCI-Paris, PSL Research University, Sorbonne Université Univ Paris 06, CNRS UMR 8213, 75005 Paris, France;* orcid.org/0000-0003-1214-6026

Josep Planelles − *Departament de Quimica Fisica i Analitica, Universitat Jaume I, E-12080 Castello de la Plana, Spain*

Hong Po − *Laboratoire de Physique et d'Etude des Matériaux, ESPCI-Paris, PSL Research University, Sorbonne Université Univ Paris 06, CNRS UMR 8213, 75005 Paris, France;* orcid.org/0000-0001-5138-4997

Eva Izquierdo − *Sorbonne Université, CNRS, Institut des NanoSciences de Paris, INSP, 75005 Paris, France*

Lina Makke − *Laboratoire de Physique et d'Etude des Matériaux, ESPCI-Paris, PSL Research University, Sorbonne Université Univ Paris 06, CNRS UMR 8213, 75005 Paris, France;* orcid.org/0000-0002-4319-5464

Charlie Gréboval − *Sorbonne Université, CNRS, Institut des NanoSciences de Paris, INSP, 75005 Paris, France;* orcid.org/0000-0002-0314-7273

Nicolas Moghaddam − *Laboratoire de Physique et d'Etude des Matériaux, ESPCI-Paris, PSL Research University, Sorbonne Université Univ Paris 06, CNRS UMR 8213, 75005 Paris, France;* orcid.org/0000-0003-2935-9386

Adrien Khalili − *Sorbonne Université, CNRS, Institut des NanoSciences de Paris, INSP, 75005 Paris, France;* orcid.org/0000-0001-5685-9963

Tung Huu Dang − *Sorbonne Université, CNRS, Institut des NanoSciences de Paris, INSP, 75005 Paris, France;* orcid.org/0000-0003-0310-9004

Audrey Chu − *Sorbonne Université, CNRS, Institut des NanoSciences de Paris, INSP, 75005 Paris, France;* orcid.org/0000-0002-6905-7131

Stefano Pierini − *Sorbonne Université, CNRS, Institut des NanoSciences de Paris, INSP, 75005 Paris, France;* orcid.org/0000-0003-1951-5357

Claire Abadie − *Sorbonne Université, CNRS, Institut des NanoSciences de Paris, INSP, 75005 Paris, France;* orcid.org/0000-0003-4309-9488

Mariarosa Cavallo − *Sorbonne Université, CNRS, Institut des NanoSciences de Paris, INSP, 75005 Paris, France;* orcid.org/0000-0002-8768-5545

Erwan Bossavit − *Sorbonne Université, CNRS, Institut des NanoSciences de Paris, INSP, 75005 Paris, France*

Xiang Zhen Xu − *Laboratoire de Physique et d'Etude des Matériaux, ESPCI-Paris, PSL Research University, Sorbonne Université Univ Paris 06, CNRS UMR 8213, 75005 Paris, France*

Philippe Hollander − *Synchrotron-SOLEIL, F91192 Gif sur Yvette, France*

Mathieu Silly − *Synchrotron-SOLEIL, F91192 Gif sur Yvette, France*

Emmanuel Lhuillier − *Sorbonne Université, CNRS, Institut des NanoSciences de Paris, INSP, 75005 Paris, France;* orcid.org/0000-0003-2582-1422

Juan I. Climente − *Departament de Quimica Fisica i Analitica, Universitat Jaume I, E-12080 Castello de la Plana, Spain*

Complete contact information is available at: https://pubs.acs.org/10.1021/acs.chemmater.1c02951

Notes

The authors declare no competing financial interest.

ACKNOWLEDGMENTS

The project was supported by ERC starting grants Ne2DeM (grant no 853049) and blackQD (grant no 756225). The authors acknowledge the use of clean-room facilities at the "Centrale de Proximité Paris-Centre". This work was

supported by Region Ile-de-France in the framework of DIM Nano-K (grant dopQD). This work was also supported by French state funds managed by the ANR within the Investissements d'Avenir programme under reference ANR-11-IDEX-0004-02 and, more specifically, within the framework of the Cluster of Excellence MATISSE and by grants IPER-Nano2 (ANR-18CE30-0023-01), Copin (ANR-19-CE24-0022), Frontal (ANR-19-CE09-0017), Graskop (ANR-19-CE09-0026), NITQuantum (ANR-20-ASTR-0008-01), Bright (ANR-21-CE24-0012-02), and MixDferro (ANR-21-CE09-0029). A.C. thanks Agence Innovation Defense for Ph.D. funding. J.P. and J.I.C. acknowledge support from Prometeo Grant Q-Devices (Prometeo/2018/098).

REFERENCES

(1) Diroll, B. T. Colloidal Quantum Wells for Optoelectronic Devices. *J. Mater. Chem. C* **2020**, *8*, 10628−10640.
(2) Nasilowski, M.; Mahler, B.; Lhuillier, E.; Ithurria, S.; Dubertret, B. Two-Dimensional Colloidal Nanocrystals. *Chem. Rev.* **2016**, *116*, 10934−10982.
(3) Lhuillier, E.; Pedetti, S.; Ithurria, S.; Nadal, B.; Heuclin, H.; Dubertret, B. Two-Dimensional Colloidal Metal Chalcogenides Semiconductors: Synthesis, Spectroscopy, and Applications. *Acc. Chem. Res.* **2015**, *48*, 22−30.
(4) Ithurria, S.; Talapin, D. V. Colloidal Atomic Layer Deposition (c-ALD) Using Self-Limiting Reactions at Nanocrystal Surface Coupled to Phase Transfer between Polar and Nonpolar Media. *J. Am. Chem. Soc.* **2012**, *134*, 18585−18590.
(5) Singh, S.; Tomar, R.; Ten Brinck, S.; De Roo, J.; Geiregat, P.; Martins, J. C.; Infante, I.; Hens, Z. Colloidal CdSe Nanoplatelets, A Model for Surface Chemistry/Optoelectronic Property Relations in Semiconductor Nanocrystals. *J. Am. Chem. Soc.* **2018**, *140*, 13292−13300.
(6) Philbin, J. P.; Brumberg, A.; Diroll, B. T.; Cho, W.; Talapin, D. V.; Schaller, R. D.; Rabani, E. Area and Thickness Dependence of Auger Recombination in Nanoplatelets. *J. Chem. Phys.* **2020**, *153*, No. 054104.
(7) Li, Q.; Lian, T. Area- and Thickness-Dependent Biexciton Auger Recombination in Colloidal CdSe Nanoplatelets: Breaking the "Universal Volume Scaling Law.". *Nano Lett.* **2017**, *17*, 3152−3158.
(8) Liu, B.; Altintas, Y.; Wang, L.; Shendre, S.; Sharma, M.; Sun, H.; Mutlugun, E.; Demir, H. V. Record High External Quantum Efficiency of 19.2% Achieved in Light-Emitting Diodes of Colloidal Quantum Wells Enabled by Hot-Injection Shell Growth. *Adv. Mater.* **2020**, *32*, No. 1905824.
(9) Qu, J.; Rastogi, P.; Gréboval, C.; Livache, C.; Dufour, M.; Chu, A.; Chee, S.-S.; Ramade, J.; Xu, X. Z.; Ithurria, S.; Lhuillier, E. Nanoplatelet-Based Light-Emitting Diode and Its Use in All-Nanocrystal LiFi-like Communication. *ACS Appl. Mater. Interfaces* **2020**, *12*, 22058−22065.
(10) Xiao, P.; Huang, J.; Yan, D.; Luo, D.; Yuan, J.; Liu, B.; Liang, D. Emergence of Nanoplatelet Light-Emitting Diodes. *Materials* **2018**, *11*, No. 1376.
(11) Grim, J. Q.; Christodoulou, S.; Di Stasio, F.; Krahne, R.; Cingolani, R.; Manna, L.; Moreels, I. Continuous-Wave Biexciton Lasing at Room Temperature Using Solution-Processed Quantum Wells. *Nat. Nanotechnol.* **2014**, *9*, 891−895.
(12) Guzelturk, B.; Kelestemur, Y.; Olutas, M.; Delikanli, S.; Demir, H. V. Amplified Spontaneous Emission and Lasing in Colloidal Nanoplatelets. *ACS Nano* **2014**, *8*, 6599−6605.
(13) Wu, M.; Ha, S. T.; Shendre, S.; Durmusoglu, E. G.; Koh, W.-K.; Abujetas, D. R.; Sánchez-Gil, J. A.; Paniagua-Domínguez, R.; Demir, H. V.; Kuznetsov, A. I. Room-Temperature Lasing in Colloidal Nanoplatelets via Mie-Resonant Bound States in the Continuum. *Nano Lett.* **2020**, *20*, 6005−6011.
(14) Schliehe, C.; Juarez, B. H.; Pelletier, M.; Jander, S.; Greshnykh, D.; Nagel, M.; Meyer, A.; Foerster, S.; Kornowski, A.; Klinke, C.; Weller, H. Ultrathin PbS Sheets by Two-Dimensional Oriented Attachment. *Science* **2010**, *329*, 550−553.
(15) Macias-Pinilla, D. F.; Echeverría-Arrondo, C.; Gualdrón Reyes, A. F.; Agouram, S.; Muñoz-Sanjosé, V.; Planelles, J.; Mora-Seró, I.; Climente, J. I. Morphology and Band Structure of Orthorhombic PbS Nanoplatelets: An Indirect Band Gap Material. *Chem. Mater.* **2021**, *33*, 420−429.
(16) Skurlov, I.; Sokolova, A.; Galle, T.; Cherevkov, S.; Ushakova, E.; Baranov, A.; Lesnyak, V.; Fedorov, A.; Litvin, A. Temperature-Dependent Photoluminescent Properties of PbSe Nanoplatelets. *Nanomaterials* **2020**, *10*, No. 2570.
(17) Bouet, C.; Laufer, D.; Mahler, B.; Nadal, B.; Heuclin, H.; Pedetti, S.; Patriarche, G.; Dubertret, B. Synthesis of Zinc and Lead Chalcogenide Core and Core/Shell Nanoplatelets Using Sequential Cation Exchange Reactions. *Chem. Mater.* **2014**, *26*, 3002−3008.
(18) Khan, A. H.; Brescia, R.; Polovitsyn, A.; Angeloni, I.; Martín-García, B.; Moreels, I. Near-Infrared Emitting Colloidal PbS Nanoplatelets: Lateral Size Control and Optical Spectroscopy. *Chem. Mater.* **2017**, *29*, 2883−2889.
(19) Izquierdo, E.; Robin, A.; Keuleyan, S.; Lequeux, N.; Lhuillier, E.; Ithurria, S. Strongly Confined HgTe 2D Nanoplatelets as Narrow Near-Infrared Emitters. *J. Am. Chem. Soc.* **2016**, *138*, 10496−10501.
(20) Gréboval, C.; Izquierdo, E.; Livache, C.; Martinez, B.; Dufour, M.; Goubet, N.; Moghaddam, N.; Qu, J.; Chu, A.; Ramade, J.; Aubin, H.; Cruguel, H.; Silly, M.; Lhuillier, E.; Ithurria, S. Impact of Dimensionality and Confinement on the Electronic Properties of Mercury Chalcogenide Nanocrystals. *Nanoscale* **2019**, *11*, 3905−3915.
(21) Livache, C.; Izquierdo, E.; Martinez, B.; Dufour, M.; Pierucci, D.; Keuleyan, S.; Cruguel, H.; Becerra, L.; Fave, J. L.; Aubin, H.; Ouerghi, A.; Lacaze, E.; Silly, M. G.; Dubertret, B.; Ithurria, S.; Lhuillier, E. Charge Dynamics and Optolectronic Properties in HgTe Colloidal Quantum Wells. *Nano Lett.* **2017**, *17*, 4067−4074.
(22) Izquierdo, E.; Dufour, M.; Chu, A.; Livache, C.; Martinez, B.; Amelot, D.; Patriarche, G.; Lequeux, N.; Lhuillier, E.; Ithurria, S. Coupled HgSe Colloidal Quantum Wells through a Tunable Barrier: A Strategy To Uncouple Optical and Transport Band Gap. *Chem. Mater.* **2018**, *30*, 4065−4072.
(23) Moghaddam, N.; Gréboval, C.; Qu, J.; Chu, A.; Rastogi, P.; Livache, C.; Khalili, A.; Xu, X. Z.; Baptiste, B.; Klotz, S.; Fishman, G.; Capitani, F.; Ithurria, S.; Sauvage, S.; Lhuillier, E. The Strong Confinement Regime in HgTe Two-Dimensional Nanoplatelets. *J. Phys. Chem. C* **2020**, *124*, 23460−23468.
(24) Tenney, S. M.; Vilchez, V.; Sonnleitner, M. L.; Huang, C.; Friedman, H. C.; Shin, A. J.; Atallah, T. L.; Deshmukh, A. P.; Ithurria, S.; Caram, J. R. Mercury Chalcogenide Nanoplatelet−Quantum Dot Heterostructures as a New Class of Continuously Tunable Bright Shortwave Infrared Emitters. *J. Phys. Chem. Lett.* **2020**, *11*, 3473−3480.
(25) Fan, F.; Kanjanaboos, P.; Saravanapavanantham, M.; Beauregard, E.; Ingram, G.; Yassitepe, E.; Adachi, M. M.; Voznyy, O.; Johnston, A. K.; Walters, G.; Kim, G.-H.; Lu, Z.-H.; Sargent, E. H. Colloidal CdSe1−XSx Nanoplatelets with Narrow and Continuously-Tunable Electroluminescence. *Nano Lett.* **2015**, *15*, 4611−4615.
(26) Tenne, R.; Pedetti, S.; Kazes, M.; Ithurria, S.; Houben, L.; Nadal, B.; Oron, D.; Dubertret, B. From Dilute Isovalent Substitution to Alloying in CdSeTe Nanoplatelets. *Phys. Chem. Chem. Phys.* **2016**, *18*, 15295−15303.
(27) Galle, T.; Kazes, M.; Hübner, R.; Lox, J.; Samadi Khoshkhoo, M.; Sonntag, L.; Tietze, R.; Sayevich, V.; Oron, D.; Koitzsch, A.; Lesnyak, V.; Eychmüller, A. Colloidal Mercury-Doped CdSe Nanoplatelets with Dual Fluorescence. *Chem. Mater.* **2019**, *31*, 5065−5074.
(28) Dufour, M.; Izquierdo, E.; Livache, C.; Martinez, B.; Silly, M. G.; Pons, T.; Lhuillier, E.; Delerue, C.; Ithurria, S. Doping as a Strategy to Tune Color of 2D Colloidal Nanoplatelets. *ACS Appl. Mater. Interfaces* **2019**, *11*, 10128−10134.
(29) Khan, A. H.; Pinchetti, V.; Tanghe, I.; Dang, Z.; Martín-García, B.; Hens, Z.; Van Thourhout, D.; Geiregat, P.; Brovelli, S.; Moreels, I. Tunable and Efficient Red to Near-Infrared Photoluminescence by

Synergistic Exploitation of Core and Surface Silver Doping of CdSe Nanoplatelets. *Chem. Mater.* **2019**, *31*, 1450−1459.
(30) Sharma, A.; Sharma, M.; Gungor, K.; Olutas, M.; Dede, D.; Demir, H. V. Near-Infrared-Emitting Five-Monolayer Thick Copper-Doped CdSe Nanoplatelets. *Adv. Opt. Mater.* **2019**, *7*, No. 1900831.
(31) Sharma, M.; Gungor, K.; Yeltik, A.; Olutas, M.; Guzelturk, B.; Kelestemur, Y.; Erdem, T.; Delikanli, S.; McBride, J. R.; Demir, H. V. Near-Unity Emitting Copper-Doped Colloidal Semiconductor Quantum Wells for Luminescent Solar Concentrators. *Adv. Mater.* **2017**, *29*, No. 1700821.
(32) Diroll, B. T.; Chen, M.; Coropceanu, I.; Williams, K. R.; Talapin, D. V.; Guyot-Sionnest, P.; Schaller, R. D. Polarized Near-Infrared Intersubband Absorptions in CdSe Colloidal Quantum Wells. *Nat. Commun.* **2019**, *10*, No. 4511.
(33) Mitrofanov, A.; Prudnikau, A.; Di Stasio, F.; Weiß, N.; Hübner, R.; Dominic, A. M.; Borchert, K. B. L.; Lesnyak, V.; Eychmüller, A. Near-Infrared-Emitting CdxHg1−XSe-Based Core/Shell Nanoplatelets. *Chem. Mater.* **2021**, *33*, 7693−7702.
(34) Lhuillier, E.; Ithurria, S.; Descamps-Mandine, A.; Douillard, T.; Castaing, R.; Xu, X. Z.; Taberna, P.-L.; Simon, P.; Aubin, H.; Dubertret, B. Investigating the N- and p-Type Electrolytic Charging of Colloidal Nanoplatelets. *J. Phys. Chem. C* **2015**, *119*, 21795−21799.
(35) Bergeard, N.; Silly, M. G.; Krizmancic, D.; Chauvet, C.; Guzzo, M.; Ricaud, J. P.; Izquierdo, M.; Stebel, L.; Pittana, P.; Sergo, R.; Cautero, G.; Dufour, G.; Rochet, F.; Sirotti, F. Time-Resolved Photoelectron Spectroscopy Using Synchrotron Radiation Time Structure. *J. Synchrotron Radiat.* **2011**, *18*, 245−250.
(36) Novik, E. G.; Pfeuffer-Jeschke, A.; Jungwirth, T.; Latussek, V.; Becker, C. R.; Landwehr, G.; Buhmann, H.; Molenkamp, L. W. Band Structure of Semimagnetic Hg_{1-y} Mn y Te Quantum Wells. *Phys. Rev. B* **2005**, *72*, No. 035321.
(37) Landolt-Börnstein—Group III Condensed Matter. In *II−VI and I−VII Compounds; Semimagnetic Compounds*; Madelung, O.; Rössler, U.; Schulz, M., Eds.; Springer-Verlag: Berlin/Heidelberg, 1999; Vol. *41B*.
(38) Pedetti, S.; Nadal, B.; Lhuillier, E.; Mahler, B.; Bouet, C.; Abécassis, B.; Xu, X.; Dubertret, B. Optimized Synthesis of CdTe Nanoplatelets and Photoresponse of CdTe Nanoplatelets Films. *Chem. Mater.* **2013**, *25*, 2455−2462.
(39) Rivest, J. B.; Jain, P. K. Cation Exchange on the Nanoscale: An Emerging Technique for New Material Synthesis, Device Fabrication, and Chemical Sensing. *Chem. Soc. Rev.* **2012**, *42*, 89−96.
(40) Jharimune, S.; Sathe, A. A.; Rioux, R. M. Solvent-Dependent Impact of Spectator Anions on the Thermodynamics of Cation Exchange in CdSe Nanocrystals. *J. Phys. Chem. C* **2021**, *125*, 12792−12801.
(41) De Trizio, L.; Manna, L. Forging Colloidal Nanostructures via Cation Exchange Reactions. *Chem. Rev.* **2016**, *116*, 10852−10887.
(42) Lim, S. J.; Kim, W.; Shin, S. K. Surface-Dependent, Ligand-Mediated Photochemical Etching of CdSe Nanoplatelets. *J. Am. Chem. Soc.* **2012**, *134*, 7576−7579.
(43) König, M.; Wiedmann, S.; Brüne, C.; Roth, A.; Buhmann, H.; Molenkamp, L. W.; Qi, X.-L.; Zhang, S.-C. Quantum Spin Hall Insulator State in HgTe Quantum Wells. *Science* **2007**, *318*, 766−770.
(44) Dai, X.; Hughes, T. L.; Qi, X.-L.; Fang, Z.; Zhang, S.-C. Helical Edge and Surface States in HgTe Quantum Wells and Bulk Insulators. *Phys. Rev. B* **2008**, *77*, No. 125319.
(45) Minkov, G. M.; Aleshkin, V. Ya.; Rut, O. E.; Sherstobitov, A. A.; Germanenko, A. V.; Dvoretski, S. A.; Mikhailov, N. N. Valence Band Energy Spectrum of HgTe Quantum Wells with an Inverted Band Structure. *Phys. Rev. B* **2017**, *96*, No. 035310.
(46) Christodoulou, S.; Climente, J. I.; Planelles, J.; Brescia, R.; Prato, M.; Martín-García, B.; Khan, A. H.; Moreels, I. Chloride-Induced Thickness Control in CdSe Nanoplatelets. *Nano Lett.* **2018**, *18*, 6248−6254.
(47) Ithurria, S.; Tessier, M. D.; Mahler, B.; Lobo, R. P. S. M.; Dubertret, B.; Efros, A. L. Colloidal Nanoplatelets with Two-Dimensional Electronic Structure. *Nat. Mater.* **2011**, *10*, 936−941.
(48) Benchamekh, R.; Gippius, N. A.; Even, J.; Nestoklon, M. O.; Jancu, J.-M.; Ithurria, S.; Dubertret, B.; Efros, A. L.; Voisin, P. Tight-Binding Calculations of Image-Charge Effects in Colloidal Nanoscale Platelets of CdSe. *Phys. Rev. B* **2014**, *89*, No. 035307.
(49) Jagtap, A.; Martinez, B.; Goubet, N.; Chu, A.; Livache, C.; Gréboval, C.; Ramade, J.; Amelot, D.; Trousset, P.; Triboulin, A.; Ithurria, S.; Silly, M. G.; Dubertret, B.; Lhuillier, E. Design of a Unipolar Barrier for a Nanocrystal-Based Short-Wave Infrared Photodiode. *ACS Photonics* **2018**, *5*, 4569−4576.
(50) Wei, S.-H.; Zunger, A. Calculated Natural Band Offsets of All II−VI and III−V Semiconductors: Chemical Trends and the Role of Cation d Orbitals. *Appl. Phys. Lett.* **1998**, *72*, 2011−2013.
(51) Amelot, D.; Rastogi, P.; Martinez, B.; Gréboval, C.; Livache, C.; Bresciani, F. A.; Qu, J.; Chu, A.; Goyal, M.; Chee, S.-S.; Casaretto, N.; Xu, X. Z.; Méthivier, C.; Cruguel, H.; Ouerghi, A.; Nag, A.; Silly, M. G.; Witkowski, N.; Lhuillier, E. Revealing the Band Structure of FAPI Quantum Dot Film and Its Interfaces with Electron and Hole Transport Layer Using Time Resolved Photoemission. *J. Phys. Chem. C* **2020**, *124*, 3873−3880.
(52) Spencer, B. F.; Leontiadou, M. A.; Clark, P. C. J.; Williamson, A. I.; Silly, M. G.; Sirotti, F.; Fairclough, S. M.; Tsang, S. C. E.; Neo, D. C. J.; Assender, H. E.; Watt, A. A. R.; Flavell, W. R. Charge Dynamics at Heterojunctions for PbS/ZnO Colloidal Quantum Dot Solar Cells Probed with Time-Resolved Surface Photovoltage Spectroscopy. *Appl. Phys. Lett.* **2016**, *108*, No. 091603.
(53) Spencer, B. F.; Cliffe, M. J.; Graham, D. M.; Hardman, S. J. O.; Seddon, E. A.; Syres, K. L.; Thomas, A. G.; Sirotti, F.; Silly, M. G.; Akhtar, J.; O'Brien, P.; Fairclough, S. M.; Smith, J. M.; Chattopadhyay, S.; Flavell, W. R. Chemically-Specific Time-Resolved Surface Photovoltage Spectroscopy: Carrier Dynamics at the Interface of Quantum Dots Attached to a Metal Oxide. *Surf. Sci.* **2015**, *641*, 320−325.

https://doi.org/10.1021/acs.chemmater.1c02951
Chem. Mater. 2021, 33, 9252−9261